

Analysis of DC Motor Current Waveforms Affecting the Accuracy of “Sensorless” Angle Measurement

Alexander Hoßfeld^{ID}, Felix Hiester^{ID}, and Ulrich Konigorski^{ID}

Abstract—A typical approach for “sensorless” angle or speed measurement of dc machines is to evaluate periodic oscillations in the electrical motor signals which is also known as ripple counting. This method is usually applied to the current signal and very susceptible to counting errors due to different waveforms caused by various influences. In this article, the steady-state current waveforms of a small dc machine are investigated to identify the causes leading to incorrect counting results. The focus is on production tolerances and changes over the service life of the motor. This is done both by the experimental and simulative investigations and analysis of the signals in the time and frequency domains. For the simulative investigation, much attention is paid to suitable modeling for this particular task and parameter variations are performed to separate the influences on the current signal. The goal is a better understanding of the different waveforms and their causes as a basis for the development of future error-free counting algorithms.

Index Terms—Current measurement, dc motors, modeling, numerical simulation, sensorless control, spectral analysis.

I. INTRODUCTION

THE reasons for choosing a “sensorless” approach are mainly cost savings and a higher robustness against disturbances [1]. Although the method is referred to as “sensorless” because there is no angle or speed sensor attached to the motor shaft, of course, at least one sensor must be present to measure an electrical signal. The literature suggests the division of “sensorless” principles into model- and ripple-based methods [2], [3]. The first involves the calculation of the speed or angle based on a mathematical motor model, whereby measured signals, such as voltage and current, serve as input variables and the knowledge of certain parameter values is required. In the second case, a distinctive periodic oscillation in the electrical motor signals, which is proportional to the speed, is evaluated. Provided that the oscillations are clearly detectable, this method is similar to the mode of operation of an incremental angle encoder but without the information about the direction of rotation. Thus, it gives independence of measurement errors and parameter deviations,

which inevitably leads to errors in the calculation result in the case of model-based methods [4], [5]. However, calculation errors can also occur with ripple-based methods if other frequencies and signal noise occur in the measurement signal in addition to the frequency to be evaluated. In contrast to speed determination, the incremental method of determining the position is complicated by the fact that counting errors add up over the course of operating time, and the deviation from the actual position value increases.

This shows that there is a need to increase the accuracy of oscillation detection, which is also taken up in the literature on ripple-based methods [2], [3], [6]–[13]. It can be stated that the knowledge of the possible occurring disturbances is mandatory for the development of an algorithm because, otherwise, its robustness cannot be guaranteed or the measurement error cannot be specified. Unfortunately, this is only sparsely considered. Typically, simple investigations of an undisturbed motor current waveform in the time or frequency domain are performed [3], [10], [13]. The frequency resolution in [3] is very low, and only the commutation frequency and its harmonics are visible in the spectrum. In [13], a higher resolution is given, where the commutation frequency can be observed as a harmonic of the rotational frequency and other rotational harmonics occur. A slightly deeper insight into the shape of an ideal oscillation, but with the remark that it may change under different circumstances, is provided in [10]. In the case of disturbed current signals, possible causes are listed but not analyzed in detail [8], [10], [12]. Deviations from the disturbed idle steady-state waveform are shown with a comparison to an applied load [7] and with a comparison to a transient state [11]. A slightly disturbed signal with its corresponding amplitude spectrum is shown in [9], and in [6], a comparison in the time and frequency domains between a qualitative good and bad motor is given. To show the course of frequency changes against time during a transient operation of the motor, a spectrogram is used in [2].

The literature review shows that there is a vast variety of possible current waveforms and that algorithm development only reacts to certain signal shapes and disturbance occurrences. This means that none of the considered algorithms can function robustly and error-free in every case because a holistic overview of possible waveforms and influencing factors is missing. This article is intended to contribute to filling this void with a detailed experimental and simulative analysis to identify the factors influencing disturbed waveforms and analyze the magnitude of their impact. This will provide a

Manuscript received August 4, 2020; revised October 1, 2020; accepted October 15, 2020. Date of publication October 30, 2020; date of current version January 4, 2021. The Associate Editor coordinating the review process was Roberto Ferrero. (Corresponding author: Alexander Hoßfeld.)

Alexander Hoßfeld and Felix Hiester are with ZF Active Safety GmbH, 56070 Koblenz, Germany (e-mail: alexander.hossfeld@zf.com; felix.hiester1@zf.com).

Ulrich Konigorski is with the Control Systems and Mechatronics Laboratory, Technical University of Darmstadt, 64283 Darmstadt, Germany (e-mail: ukonigorski@iat.tu-darmstadt.de).

Digital Object Identifier 10.1109/TIM.2020.3034598

1557-9662 © 2020 IEEE. Personal use is permitted, but republication/redistribution requires IEEE permission.
See <https://www.ieee.org/publications/rights/index.html> for more information.

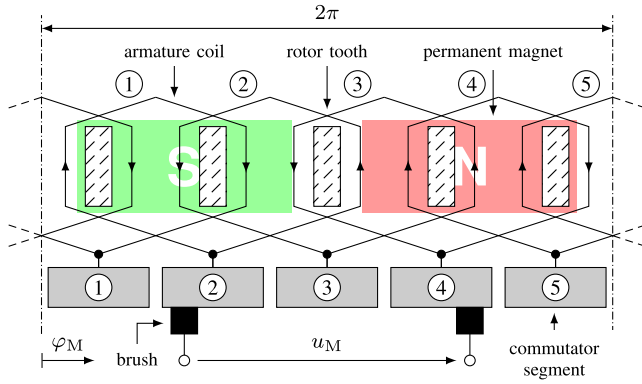


Fig. 1. Winding diagram of the investigated motor.

basis for the development of more robust ripple counting algorithms. For this purpose, in Section II, the measured current waveforms of a small dc machine are analyzed. Section III describes the development of a detailed simulation model of this motor. In Section IV, the simulation results calculated with the software MATLAB/SIMULINK are compared with the measured values and different parameter variations are performed.

II. ANALYSIS OF MEASURED CURRENT WAVEFORMS

The motor used for the investigation is a permanent magnet direct current machine (PMDC) with a nominal power of approximately 100 W. This motor has one pair of poles and a retrogressive simplex lap winding. The winding is chorded with a pitch factor of 4/5 and the number of rotor slots and commutator segments is five each. The brushes are covering a maximum of two adjacent commutator segments depending on the angular position of the rotor. For clarification, the winding diagram of the motor is shown in Fig. 1 illustrating the brushes, commutator segments, armature coils, rotor teeth, and permanent magnets. The degree of rotational freedom φ_M , the voltage at the motor terminals u_M , and the resulting current flow at the coils are also displayed.

The motors are operated in idle speed without mechanical load to avoid influences by external disturbances. The voltage drop at the motor terminals, the current, and the angle of rotation are measured and recorded with a digital storage oscilloscope. The tests are carried out at room temperature, whereby the direction of rotation and the constant supply voltage u_S (in steps of 9, 12, and 16 V) are varied, thus achieving different speeds. In addition, new and used motors are examined, characterized by approximately 50 operating hours with an alternating direction of rotation. From each wear condition, three motor samples are selected, which are consecutively numbered 1–3. The following evaluation will be limited to the measured current signals only since the ripple is much more obvious here than in the voltage signals.

It should be noted that the specified motor angle on the abscissa axes of the shown measurement data only describes an arbitrary relative angular change and not an absolute position since no reference mark is available on the encoder. This also makes it necessary to align the data sets of different

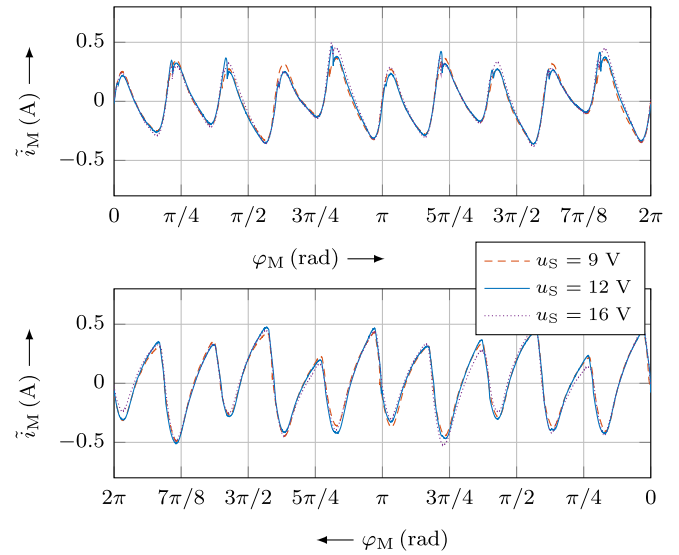


Fig. 2. Measured alternating motor currents of new sample no. 2 (top: CCW/bottom: CW).

experiments to each other. For this purpose, the sampling rate is converted in proportion to the angle of rotation with subsequent cross-correlation. Thus, a direct comparison of individual amplitudes in the following figures may be faulty, but, for an impression of how the separate experiments behave in relation to each other, this procedure is sufficient.

Fig. 2 shows the ac component \tilde{i}_M of the current signal of one revolution in dependence of the supply voltage u_S and the direction of rotation. For a “sensorless” determination of the motor angle, such periodic waveforms are ideal since the expected ten zero crossings or peaks per revolution due to the commutation process can be counted very easily. The waveforms have a regular repeating pattern and the shape of the ripples is basically similar for the same direction of rotation. A change in the direction of rotation results in a reversal of the signal shape. Furthermore, the measured values in the upper plot show additional small peaks in the range of the maximum amplitude, which is caused by the end of the commutation process.

Comparing all three test samples of the new condition in Fig. 3, it can be seen that the characteristic sawtooth shape of the signal is preserved, but there are differences in the individual amplitude heights. Thus, there seem to be constructive differences between the samples that cause the deviations. Whether these are due to production tolerances or different running-in behaviors cannot be assessed at this point. However, a disassembly has shown that all three motors have undergone a balancing process, which has led to different materials’ removal on the outer surface of the rotor and, thus, influences the magnetic flux in the air gap. Also, this represents the greatest difference between the individual samples from a manufacturing or geometric point of view.

The signal property of the sawtooth shape can no longer be observed when looking at a used sample in Fig. 4. The information about the angle of rotation contained in the signal is now much more difficult to detect, and in comparison with Fig. 2, it is noticeable that the approximate congruence with

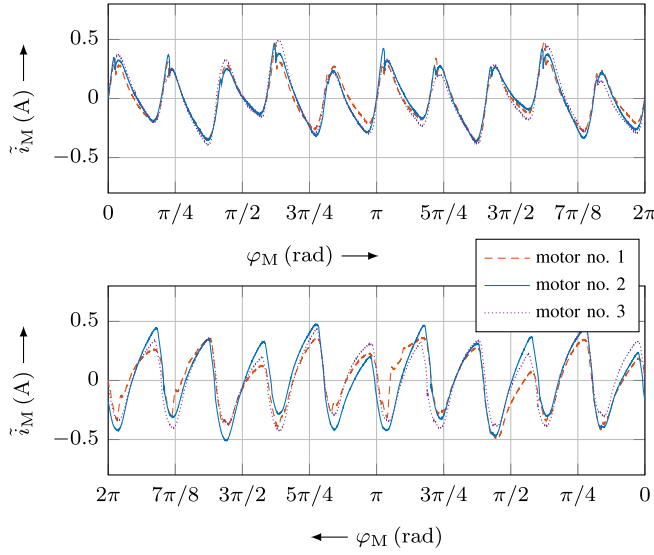


Fig. 3. Measured alternating motor currents of all new samples at $u_S = 12$ V (top: CCW/bottom: CW).

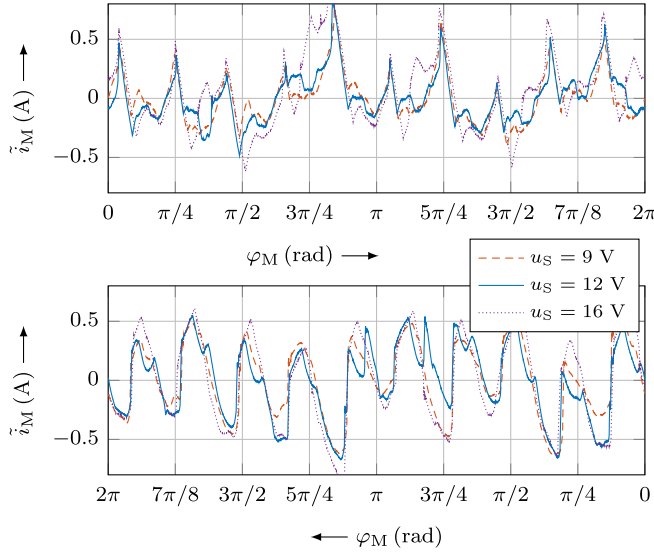


Fig. 4. Measured alternating motor currents of used sample no. 3 (top: CCW/bottom: CW).

the variation of the supply voltage has decreased. Furthermore, the inversion of the signal shape is no longer given when the direction of rotation is reversed.

The analyses carried out in the time domain so far are now to be extended by consideration in the frequency domain to obtain information about the spectral components of the signals. Apart from sporadically occurring disturbances, a stationary state can be assumed due to the otherwise valid periodicity between the engine revolutions, and thus, a spectral analysis of the idling phase can be carried out using a fast Fourier transform (FFT). It applies to all tests performed that the expected ripple frequency of ten times the rotational frequency f_M is always contained in the spectrum and only its amplitude varies. This fact is shown in Fig. 5 by comparing the new and used conditions according to the time series in Figs. 2 and 4. For the new condition, considered as an ideal ripple shape

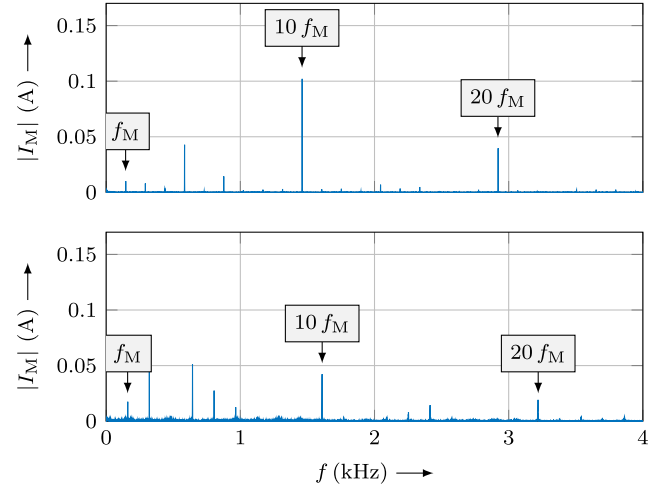


Fig. 5. Amplitude spectra of measured motor currents ($u_S = 12$ V/CCW/top: new, no. 2/bottom: used, no. 3).

for “sensorless” angle determination, the upper plot shows a clear maximum with the ripple frequency at approximately 1.45 kHz. Furthermore, the first harmonic of this frequency and four and six times the rotational frequency with lower amplitude are clearly visible. For the used condition, the spectral analysis in the lower plot shows a considerably reduced amplitude of the ripple frequency resulting in a changed ratio with the other frequency components. Especially, the harmonics at two and four times the rotational frequency show a slightly higher amplitude, which makes it difficult to identify the angle of rotation in the time domain.

III. DEVELOPMENT OF A DETAILED SIMULATION MODEL

Typically, a permanent magnet dc motor is modeled as a system with one electrical and one mechanical degree of freedom, resulting in a system of two coupled differential equations, which is

$$\frac{d}{dt} \begin{bmatrix} i_M \\ \omega_M \end{bmatrix} = \begin{bmatrix} -R_M/L_M & -k\Phi/L_M \\ k\Phi/J_M & -d/J_M \end{bmatrix} \begin{bmatrix} i_M \\ \omega_M \end{bmatrix} + \begin{bmatrix} 1/L_M & 0 \\ 0 & -1/J_M \end{bmatrix} \begin{bmatrix} u_M \\ M_L \end{bmatrix} \quad (1)$$

in the state-space representation [14]–[18]. The state variables consist of the motor current i_M and the angular velocity ω_M . The total inner resistance R_M , the self-inductance L_M , the magnetic air gap flux per pole Φ , and the motor constant k appear as electrical and magnetic parameters. The mechanical subsystem contains the mass moment of inertia J_M and an assumption of speed-proportional damping d . The motor voltage u_M and the load torque M_L act on the overall system as input variables. This type of modeling is used, for example, to investigate the dynamic behavior or for controller design, but it is not suitable to describe the ripples in the motor current signal, which is why a more detailed modeling must be carried out. Existing models in the literature, such as [19]–[25], model, for example, all rotor coils, commutator segments, and brushes individually but are usually used to investigate the commutation behavior. In the following, a similar approach is chosen.

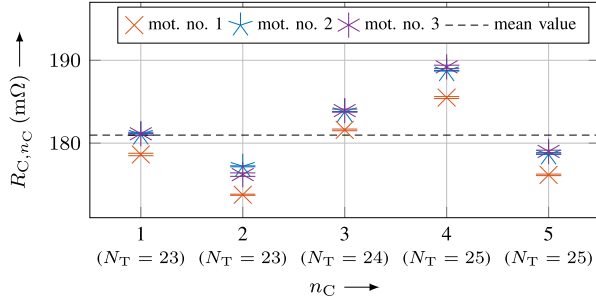


Fig. 6. Measured coil resistances of all new samples.

A. Coil Resistance

The continuously distributed resistance of a coil can be calculated to a discrete value according to

$$R_{C,n_C} = \rho \frac{l_{C,n_C}}{A} \quad (2)$$

where ρ is the specific resistance of the material, l_{C,n_C} is the length, and A is the cross-sectional area of the conductor. It should be noted that, depending on the winding, deviations between the individual coils may occur, for example, due to the increase in conductor length at the end turns [22]. This can also be seen in the measurement of the coil resistances of the new samples in Fig. 6, where the manufacturing process of the winding starts at coil 5 and ends at coil 1. To compensate for the resulting imbalance of the rotor, coils 4 and 5 have one turn more, and coils 1 and 2 have one turn less than the nominal number of turns, which is $N_T = 24$. The values of the used test samples do not display any deviations from the data presented and are, therefore, not shown.

B. Electromagnetic Induction

The voltage induced in an armature coil is equal to the time derivative of the total magnetic flux that passes through it, which is also known as flux linkage and the sum of the magnetic fluxes through the individual conductor turns [26]. The causes of magnetic flux through a coil in this motor design are the permanent magnets in the stator and the currents through the individual armature coils. These can be further separated into self and mutual inductances [27]. Due to the relative movement between stator and armature, an additional variable parameter in the magnetic circuit is the size of the air gap, which influences the magnetic resistance and is dependent, for example, on the aforementioned mass removal during balancing and the static and dynamic eccentricity of the rotor. However, this influence is to be neglected for now and will be dealt with later in Section IV. Thus, the total magnetic flux Ψ_{C,n_C} through a coil can be formulated as a function of the angle of rotation φ_M and the currents of the individual coils i_{C,n_C} . The induced voltage as its time derivative is calculated as

$$\begin{aligned} u_{i,C,n_C} &= \frac{d}{dt} \Psi_{C,n_C}(\varphi_M(t), i_{C,1}(t), \dots, i_{C,5}(t)) \\ &= \frac{\partial \Psi_{C,n_C}}{\partial \varphi_M} \frac{d\varphi_M}{dt} \\ &\quad + \frac{\partial \Psi_{C,n_C}}{\partial i_{C,1}} \frac{di_{C,1}}{dt} + \dots + \frac{\partial \Psi_{C,n_C}}{\partial i_{C,5}} \frac{di_{C,5}}{dt}. \end{aligned} \quad (3)$$

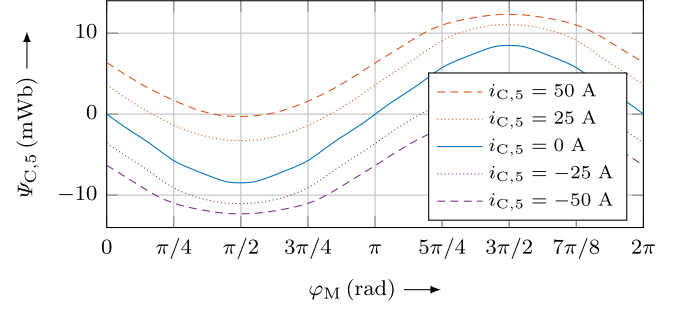


Fig. 7. Calculated total magnetic flux under the variation of the coil current.

The determination of the total magnetic flux is done by a numerical field calculation using the software ANSYS MAXWELL/RMXPRT and a 2-D motor model. In view of a desired short simulation time of the model to be developed, the simulations of magnetic and electric circuits are not coupled. Therefore, the magnetic flux is calculated in advance and stored in lookup tables. Fig. 7 shows, exemplarily, the magnetic flux of the fifth coil as a function of the angle of rotation and the influence of self-induction, whereby the number of turns was set to the nominal value of 24. The sinusoidal course over one rotor revolution reflects the number of pole pairs, whereby the minima and maxima describe the position directly below the poles. As the coil current increases, the saturation of the magnetic circuit is shown by the slower increasing average value and the decreasing oscillation width.

C. Commutation and Brush Contact

The influences on the brush-commutator contact are manifold, such as the material pairing used, its surface condition, normal force, temperature, or humidity. Detailed descriptions and investigations can be found, for example, in [22], [25], and [28]. Due to a large number of influences, there are also innumerable types of modeling attempts in the literature although a generally valid procedure with a good model quality does not seem to exist so far. The simplest type of modeling is shown in Fig. 8 and provides an antiproportional dependence of the contact resistance on the apparent contact area. This results in a trapezoidal conductance function for each possible brush contact as a function of the angle of rotation. The maximum value at full overlap is to be specified, and rise and fall at partial overlap are determined by this value and the geometry. This type of modeling is used in [29] and [30], as well as under certain adaptations in [21]–[23], and [25]. Comparisons of the basic variant of this modeling with measured values of the actual resistance curve in [19] and [22] show little agreement. Therefore, this simple contact model is extended by scaling factors at specific angle-dependent points to achieve a realistic behavior, similar to the procedure in [25].

For the geometrical description of the commutation process, the contact angles plotted on the abscissa axes in Fig. 8 are used. According to the dimensions given, the angle of the brush contact with radial alignment in relation to the commutator is

$$\varphi_{c,B} = 2 \arcsin\left(\frac{w_B}{d_s}\right) \quad (4)$$

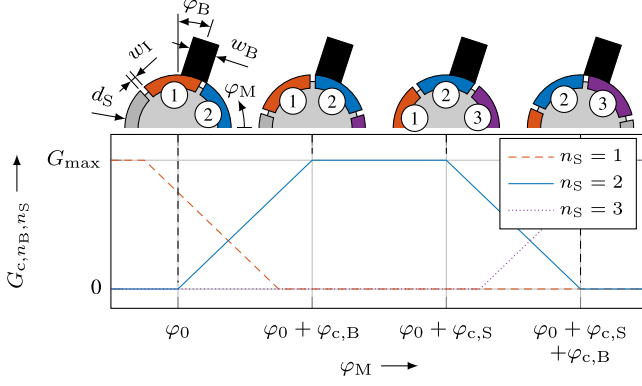


Fig. 8. Conductance functions between brushes and commutator segments.

and the angle of the commutator segment contact is

$$\varphi_{c,S} = \frac{2\pi}{5} - 2 \arcsin\left(\frac{w_1}{d_S}\right). \quad (5)$$

It should be noted that the apparent contact area to be taken into consideration for defining the brush width is significantly smaller than the actual brush width when the brushes are not run in. Furthermore, a shifting of the brushes from the neutral position to the exciting field by the angle φ_B is taken into account. Since the brushes are clamped in leg holders in the present case and, thus, move on a circular path, this angle is variable depending on the wear of the brushes and over the service life of the motor. In addition, due to the way the brushes are fixed in the leg holders and the frictional forces caused by rotation, tilting can occur depending on the direction of rotation.

D. Complete System

For the mathematical description of the complete system, the switching processes at the commutator must first be considered in a special way since different equivalent circuit diagrams of the electrical circuit can be defined depending on the angular position of the rotor. In order to avoid a discontinuous system description, a modeling option is used, which defines an equivalent system in which all commutator segments are connected to the voltage source via variable contact resistances as in [19] and [25]. Depending on the angle of rotation, the resistances at the currently noncontacting segments are assigned values that are much higher than the contact resistance to the brushes, which makes the resulting current flow negligible. This results in the equivalent circuit diagram shown in Fig. 9 for the winding diagram shown in Fig. 1.

Together with the definition of the induced voltage according to (3), the mesh rule per armature coil gives

$$\begin{aligned} u_M = & R_{C,n_C} i_{C,n_C} + u_{c,+n_S} + u_{c,-n_S+1} \\ & + \frac{\partial \Psi_{C,n_C}}{\partial \varphi_M} \frac{d\varphi_M}{dt} + \frac{\partial \Psi_{C,n_C}}{\partial i_{C,1}} \frac{di_{C,1}}{dt} \\ & + \dots + \frac{\partial \Psi_{C,n_C}}{\partial i_{C,5}} \frac{di_{C,5}}{dt} \end{aligned} \quad (6)$$

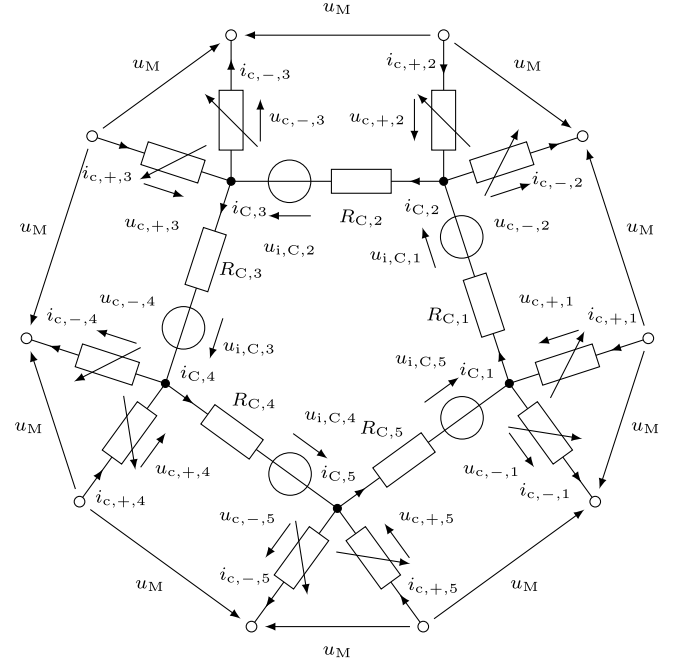


Fig. 9. Equivalent circuit diagram of the investigated motor.

and for the complete system in matrix form rearranged according to the time derivatives of the coil currents

$$\frac{\partial \Psi_C}{\partial i_C} \frac{d}{dt} i_C = \mathbf{1} u_M - u_{c,+} - u_{c,-} - R_C i_C - \frac{\partial \Psi_C}{\partial \varphi_M} \frac{d\varphi_M}{dt}. \quad (7)$$

It can be seen that the matrix $\partial \Psi_C / \partial i_C$ is fully occupied, with the main diagonal representing the self-inductances and the remaining elements the mutual inductances. A direct implementation of these equations in MATLAB/SIMULINK results in an algebraic loop since all state derivatives are coupled together. Multiplying the entire equation in

$$\frac{d}{dt} i_C = \left(\frac{\partial \Psi_C}{\partial i_C} \right)^{-1} \left(\mathbf{1} u_M - u_{c,+} - u_{c,-} - R_C i_C - \frac{\partial \Psi_C}{\partial \varphi_M} \frac{d\varphi_M}{dt} \right) \quad (8)$$

by the inverse of the matrix solves this problem, and by resolving the right-hand side of this equation, the state-space representation of the system can be derived. The remaining unknown contact voltage is calculated by resolving the mesh and junction rule at the commutator segments to avoid another algebraic loop.

IV. SIMULATION RESULTS AND COMPARISON WITH MEASUREMENT DATA

As with the previous experimental investigation, the following analysis will relate to the idling operation of the motor. First, a nominal behavior is to be achieved with the simulation model, which is why all coils, commutator segments, and brushes are assumed to be identical in their electrical or mechanical behavior, and the rotor is arranged concentrically to the stator. For a comparison with the measured data, therefore, only the sawtooth-like shape of the current waveform with a corresponding mean amplitude height

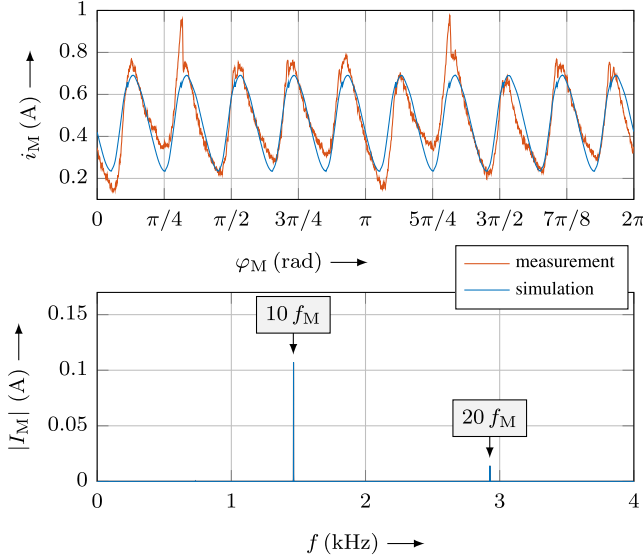


Fig. 10. Comparison of measured and simulated motor current (new/no. 1/ $u_S = 12$ V/CCW).

is relevant. This is shown in the upper part of Fig. 10 for a new motor and can be judged as good according to the requirements placed on the model and taking into account the variance of the test samples according to Fig. 3. The lower part shows the corresponding amplitude spectrum of the simulated current signal, which contains only the ripple frequency and its first harmonic. In comparison to the analysis of the measured signals in Fig. 5, no harmonic components of the rotational frequency are included, which do not correspond to the ripple frequency or its multiples. This is due to the fact that the amplitude heights in the simulated signal over one revolution are constant due to the assumed identity of all coils, commutator segments, and brushes, and the concentricity of rotor and stator.

Further considerations and analyses will refer to this simulated nominal behavior by parameter variations. In this way, deviations due to, for example, manufacturing tolerances or wear and tear and the associated more precise mapping of specific effects observable in the measurement data are considered. If the coil resistances and number of turns are changed from the initially uniformly assumed average values to the actual values (see Fig. 6), Fig. 11 shows in the upper plot clear deviations in the individual amplitude heights in comparison to the nominal behavior. The associated amplitude spectrum shows additional frequency components at the points of 2, 4, 6, and 14 times the rotational frequency, which can also be observed in the experimental investigation in Fig. 5.

As a further deviation from the nominal behavior, the effect of dynamic eccentricity e_{dyn} of the rotor is investigated. This can be caused, for example, by deformation or imbalance of the rotor and is shown for a value of 0.05 mm in Fig. 12. As before, differences in the individual amplitude heights and additional frequency components in the amplitude spectrum are observable, which are also present in the measurement data. In addition, with this analysis, it is possible to estimate the effects of rotor balancing by material removal since,

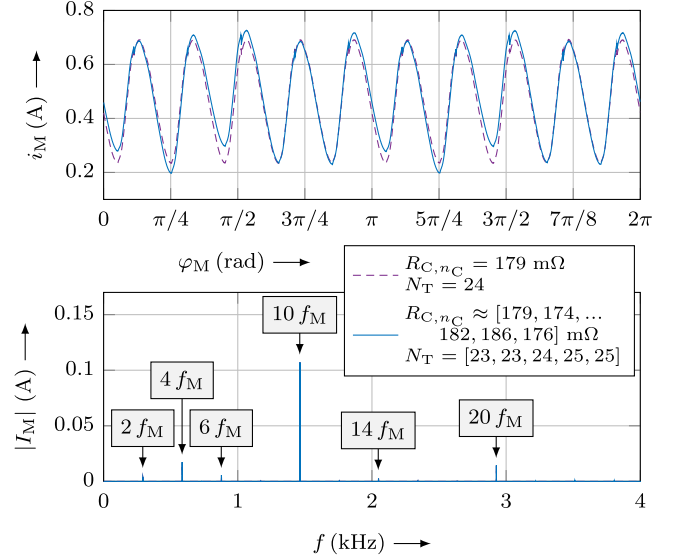


Fig. 11. Simulated motor currents under the variation of coil resistances and the number of turns ($u_S = 12$ V/CCW).

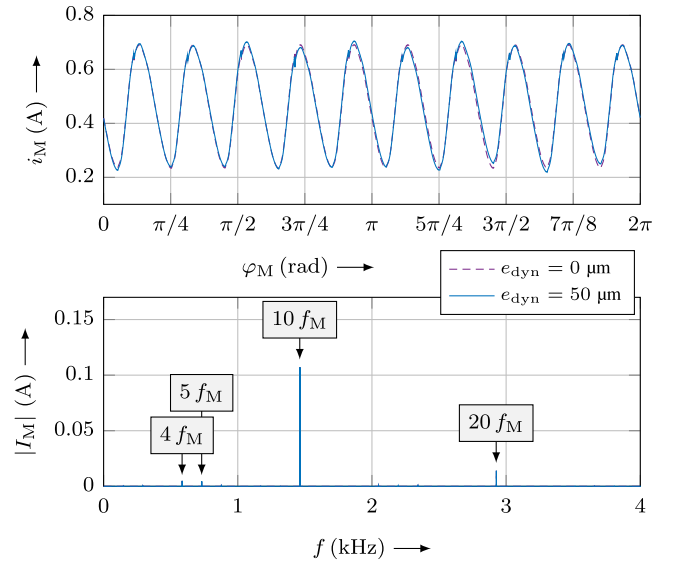


Fig. 12. Simulated motor currents under the variation of the dynamic eccentricity ($u_S = 12$ V/CCW).

as with dynamic eccentricity, a different air gap is created per rotor tooth, which rotates constantly at the angular velocity. Because the simulation result also shows different amplitude heights, such as the measurement data of the individual test samples in Fig. 3, the initial assumption that the balancing process is the cause for these deviations is substantiated.

For the brush contact, its displacement from the neutral position (see Fig. 8) is to be investigated as an influencing parameter. In Fig. 13, an arbitrarily selected opposite angle difference of $\pm 1^\circ$ to the reference value is used for this purpose, which can occur, for example, due to production-related tolerances or different wear behavior. In the upper plot, an amplitude height alternating with half the ripple frequency is shown, which also changes if the two angle values are interchanged and increases as the angle values increase. In addition to this frequency, its

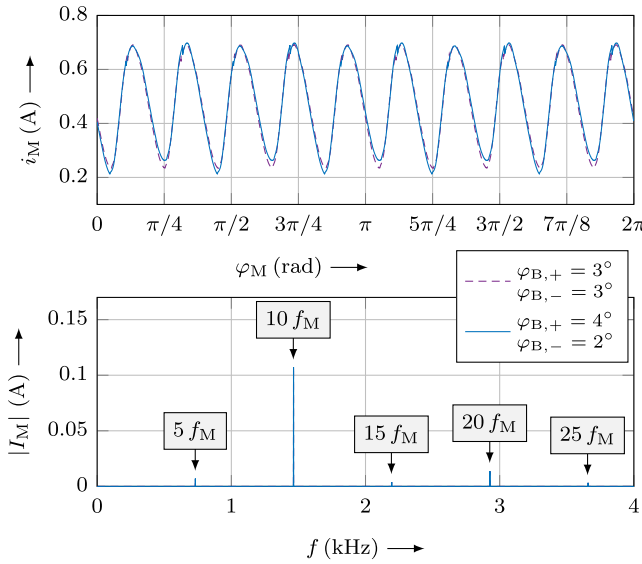


Fig. 13. Simulated motor currents under the variation of the brush shift ($u_S = 12$ V/CCW).

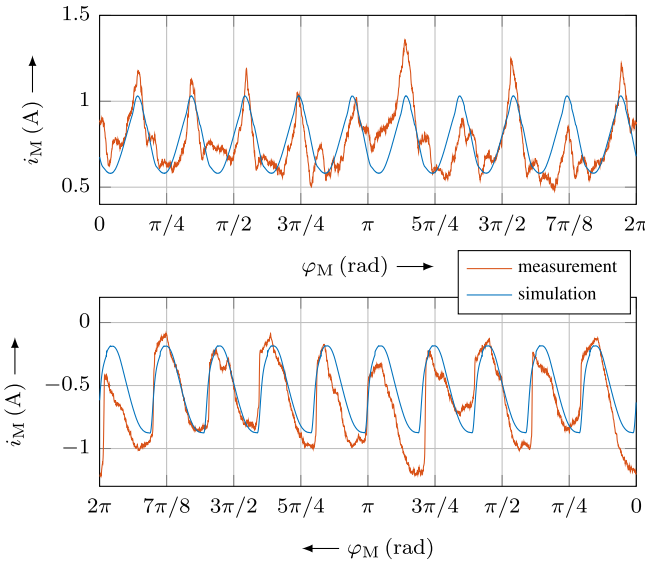


Fig. 14. Comparison of the measured and simulated motor current (used/no. 3/ $u_S = 9$ V/top: CCW/bottom: CW).

harmonics appear in the associated spectrum with decreasing amplitude, which also corresponds to the measured values in Fig. 5.

It must be noted that the simultaneous application of parameter variations does not necessarily lead to a superposition of the individual amplitude spectra. For example, if the number of turns and the brush shift are taken into account at the same time, the rotational frequency appears additionally in the spectrum (not shown) since the combination of these two parameter changes means that identical system states no longer exist in one revolution. If all the spectral analyses carried out previously are taken into account, it can be seen that all relevant frequencies of the measurement data in Fig. 5, i.e., 1, 2, 4, 5, 6, 10, 14, 15, and 20 times the rotational frequency, are represented. In addition, under some restrictions, even

individual frequency components can be assigned to a possible cause. In this case, however, it should be noted that other parameter changes that are not considered here can also cause similar frequency behavior, such as, for example, differences in the individual brush and commutator segment widths.

As a final investigation, the changes caused by brush wear over the service life of the motor are considered. Therefore, according to the explanations in Section III, the model parameters w_B and φ_B are adjusted to the values of the used motors. Fig. 14 shows the simulation results in comparison to the measured data in both directions of rotation. It can be seen that the simulated waveform changes significantly and follows the fundamental shape of the measured signals. The details of the measurements cannot be reproduced due to the lack of a proper brush contact model.

V. CONCLUSION

The experimental investigation showed significant differences between the current waveforms of new and used motors. This change in behavior can have a major impact on the accuracy of ripple counting algorithms and must be taken into account in the development process of such algorithms. An analysis of these signals in the frequency domain showed that the presence of other rotational harmonics with a similar or higher amplitude than the commutation frequency is the cause for the disturbances in the time domain. For an analysis of these harmonics, a detailed simulation model was developed. Through parameter variations, all relevant frequencies could be reproduced and possible causes for their occurrence could be identified. Unfortunately, the influence of the brush contact due to wear, which seems to have a major impact according to the measurement data, could not be investigated in detail. In addition to this, load influences, control by pulse-width modulation, or electromagnetic interference may also play an important role and be the subject of further research.

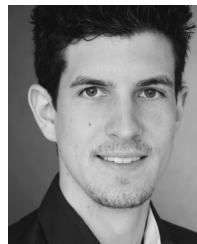
REFERENCES

- [1] H.-D. Stölting, E. Kallenbach, and W. Amrhein, *Handbook Fractional-Horsepower Drives*. Berlin, Germany: Springer, 2008.
- [2] M. Hilairet and F. Auger, "Speed sensorless control of a DC-motor via adaptive filters," *IET Electr. Power Appl.*, vol. 1, no. 4, pp. 601–610, Jul. 2007.
- [3] J. M. Knezevic, "Low-cost low-resolution sensorless positioning of DC motor drives for vehicle auxiliary applications," *IEEE Trans. Veh. Technol.*, vol. 62, no. 9, pp. 4328–4335, Nov. 2013.
- [4] S. Rajaram and S. Murugesan, "A new method for speed Measurement/Control of DC motors," *IEEE Trans. Instrum. Meas.*, vol. 27, no. 1, pp. 99–102, Mar. 1978.
- [5] O. Aydogmus and M. F. Talu, "Comparison of extended-Kalman- and particle-filter-based sensorless speed control," *IEEE Trans. Instrum. Meas.*, vol. 61, no. 2, pp. 402–410, Feb. 2012.
- [6] N. P. Oechsner and W. Bass, "Verfahren und Vorrichtung zur Messung der Drehzahl eines Gleichstrom-Kommutatormotors," German Patent Appl. 19915 875 A1, Nov. 23, 2000.
- [7] A. Consoli, G. Bottiglieri, R. Letor, R. Ruggeri, A. Testa, and S. De Caro, "Sensorless position control of DC actuators for automotive applications," in *Proc. IEEE Ind. Appl. Conf.*, Seattle, WA, USA, Oct. 2004, pp. 1217–1224.
- [8] R. Letor, A. Testa, and S. De Caro, "Estimation of the shaft position on low-cost DC actuators," in *Proc. IEEE Int. Symp. Ind. Electron.*, Bari, Italy, Jul. 2010, pp. 440–445.
- [9] R. M. Ramli, N. Mikami, and H. Takahashi, "Adaptive filters for rotational speed estimation of a sensorless DC motor with brushes," in *Proc. 10th Int. Conf. Inf. Sci.*, Kuala Lumpur, Malaysia, May 2010, pp. 562–565.

- [10] E. Vazquez-Sanchez, J. Gomez-Gil, J. C. Gamazo-Real, and J. F. Diez-Higuera, "A new method for sensorless estimation of the speed and position in brushed DC motors using support vector machines," *IEEE Trans. Ind. Electron.*, vol. 59, no. 3, pp. 1397–1408, Mar. 2012.
- [11] H. Song, W. Shi, C. Huang, and G. Lei, "Research on a new method of indirect velocity measurement for DC motors," *Sensors Transducers*, vol. 158, no. 11, pp. 262–267, Nov. 2013.
- [12] A. Testa, S. De Caro, T. Scimone, and R. Letor, "Pulse counting sensorless detection of the shaft speed and position of DC motor based electromechanical actuators," *J. Power Electron.*, vol. 14, no. 5, pp. 957–966, Sep. 2014.
- [13] S. Lu, Y. Qin, J. Hang, B. Zhang, and Q. Wang, "Adaptively estimating rotation speed from DC motor current ripple for order tracking and fault diagnosis," *IEEE Trans. Instrum. Meas.*, vol. 68, no. 3, pp. 741–753, Mar. 2019.
- [14] M. Glöckler, *Simulation Mechatronischer Systeme: Grundlagen und Technische Anwendung*. Wiesbaden, Germany: Springer Vieweg, 2014.
- [15] H.-J. Gevatter, *Handbuch der Mess- und Automatisierungstechnik im Automobil: Fahrzeugelektronik, Fahrzeugmechatronik*, 2nd ed. Berlin, Germany: Springer, 2006.
- [16] A. Binder, *Elektrische Maschinen und Antriebe: Grundlagen, Betriebsverhalten*, 2nd ed. Berlin, Germany: Springer Vieweg, 2017.
- [17] D. Schröder, *Elektrische Antriebe: Grundlagen*, 6th ed. Berlin, Germany: Springer Vieweg, 2017.
- [18] D. Schröder, *Elektrische Antriebe: Regelung von Antriebssystemen*, 4th ed. Berlin, Germany: Springer Vieweg, 2015.
- [19] R. Schröder and K. Oberreil, "Neues Verfahren zur Berechnung der Kommutierung von Gleichstrommaschinen unter Berücksichtigung der Bürstenübergangswiderstände," *Archiv für Elektrotechnik*, vol. 73, no. 2, pp. 69–79, Mar. 1990.
- [20] M. Doppelbauer, "Neue Erkenntnisse über die Kommutierung von Gleichstrommaschinen aus Anwendung der Oberfeldtheorie," (in German), *Electr. Eng.*, vol. 80, no. 1, pp. 41–50, Feb. 1997.
- [21] A. Vauquelin, J.-P. Vilain, S. Vivier, N. Labbe, and B. Dupeux, "A new modelling of DC machines taking into account commutation effects," in *Proc. 18th Int. Conf. Electr. Mach.*, Vilamoura, Portugal, Sep. 2008, pp. 1–6.
- [22] T. Heidrich, "Kommutierungsberechnung bei permanentmagneterngetten Kommutatormotoren kleiner Leistung," (in German), Ph.D. dissertation, Institut für elektrische Energie- und Steuerungstechnik, Fachgebiet Kleinmaschinen, Technische Univ. Ilmenau, Germany, 2011. [Online]. Available: <https://www.tu-ilmenau.de/ees-km/>
- [23] R. Andreux, J. Fontchastagner, N. Takorabet, N. Labbe, and J.-S. Metral, "A general approach for brushed DC machines simulation using a dedicated field/circuit coupled method," *Prog. Electromagn. Res.*, vol. 145, pp. 213–227, Dec. 2014.
- [24] H. Shen, Q. Lei, and W. Chen, "Modeling and simulation for micro DC motor based on simulink," in *Proc. Conf. Series*, Changsha, China, Jun. 2017, pp. 1–5.
- [25] C. Wolz, "Ein schnelles und genaues Simulationsmodell für permanentmagneterngette Kommutatormotoren kleiner Leistung mit Zahnspulen unter Berücksichtigung nichtlinearer Eigenschaften," Ph.D. dissertation, Institut für Energie und Automatisierungstechnik, Fachgebiet Elektrische Antriebstechnik, Technische Univ., Berlin, Berlin, Germany, 2017. [Online]. Available: <https://verlag.tu-berlin.de/dissdb/?filter%5Bsearch%5D=wolz>
- [26] E. Bolte, *Elektrische Maschinen: Grundlagen, Magnetfelder, Erwärmung, Funktionsprinzipien, Betriebsarten, Einsatz, Entwurf, Wirtschaftlichkeit*, 2nd ed. Berlin, Germany: Springer Vieweg, 2018.
- [27] G. Möller, K. Vogt, and B. Ponick, *Berechnung Elektrischer Maschinen*, 6th ed. Weinheim, Germany: Wiley, 2008.
- [28] E. Vinaricky, *Elektrische Kontakte, Werkstoffe und Anwendungen: Grundlagen, Technologien, Prüfverfahren*, 3rd ed. Berlin, Germany: Springer Vieweg, 2016.
- [29] M. Stiebler, "Ein Verfahren zur Berechnung der Kommutierungsströme und Bürstenspannungen von Gleichstrommaschinen," (in German), *Archiv für Elektrotechnik*, vol. 66, nos. 5–6, pp. 309–316, Sep. 1983.
- [30] T. Heidrich, "Analyse und Simulation des Motorstromes von Kommutatormotoren mit Permanentmagneterngetten," in *Proc. Inf. Technol. Electr. Eng.*, Ilmenau, Germany, Sep. 2006, p. 51.



Cologne, Germany. He is currently a Doctoral Candidate with ZF Active Safety GmbH, Koblenz, Germany.



Felix Hiester received the B.Eng. and M.Eng. degrees in mechanical engineering from the University of Applied Sciences Koblenz, Koblenz, Germany, in 2016 and 2018, respectively.

He is currently a CAE-Project Engineer with ZF Active Safety GmbH, Koblenz, with a focus on structural dynamics and electromagnetic simulations and analysis.



Ulrich Konigorski received the Dipl.-Ing. degree in electrical engineering and the Ph.D. degree in control theory from the University of Karlsruhe, Karlsruhe, Germany, in 1983 and 1987, respectively.

He was a Group Leader with Robert Bosch GmbH, Schwieberdingen, Germany, from 1988 to 1991, with the responsibility for the development and application of control systems for electrical power steering and hydraulic rear-wheel steering. From 1991 to 1994, he was the Head of the Sensor and Control Systems Department, Thyssen-Henschel, New Transport Technologies, Munich, Germany, and involved in the development of digital sensor and control systems for the transrapid high-speed magnetic railway. Since 1994, he has been a Professor with the Chair of Control Engineering and Electronics, Institute of Electrical Information Technology, Clausthal University of Technology, Clausthal-Zellerfeld, Germany. Since 2004, he has been a Professor with the Technical University of Darmstadt, Darmstadt, Germany, and also the Head of the Control Systems and Mechatronics Laboratory.